Transient shape variation and inner flow field of a rotating two-lobed liquid droplet

Tadashi Watanabe
Research Institute of Nuclear Engineering, University of Fukui, Kanawa-cho 1-3-33, Tsuruga-shi, Fukui-ken 914-0055, Japan

(Received 15 March 2020; accepted 17 July 2020; published 20 August 2020)

Levitated liquid droplets are not in contact with containers, and rotating two-lobed droplets are used for measuring the viscosities of molten material. In order to discuss the characteristics of two-lobed droplets, the transient shape variation and the inner flow field of a rotating liquid droplet are simulated numerically in this study. The calculated two-lobed shapes are shown to agree with the existing experimental and calculated results obtained under steady-state conditions. It is also shown that the relation between the maximum deformation and the rotation rate agrees with the experimental results. It is found that two vortices appear in the two-lobed droplet and the countercurrent flow is formed in between two lobes. The relation between the maximum deformation and the rotation rate is affected by the surface tension and the density, and the effect of density becomes small as the deformation increases. In contrast, the relation between the deformation parameter based on the minimum diameter and the aspect ratio is not affected by the droplet properties.

DOI: 10.1103/PhysRevFluids.5.083607

I. INTRODUCTION

A levitated liquid droplet is used for measuring thermophysical properties of molten materials, since the levitated material is not in contact with containers or crucibles, and the effect of the container wall is eliminated for precise measurement. Electromagnetic levitation is one of the levitation techniques for liquid metal since the Lorentz force compensates the gravitational force and the temperature is controlled by inductive heating. The surface tension of liquid metals has been measured [1–3], which can give access to the surface contamination [4]. The effect of magnetic field also has been discussed [5]. The liquid oscillation characterization can also enable the measurement of the molten metal properties, whether under standard gravitation conditions or under microgravity conditions [6,7]. The oscillation frequency has been studied theoretically [8,9] and numerical simulations have been performed [10,11]. Diamagnetic levitation, in which the magnetogravitational potential is used to levitate large spherical droplets, has been used to observe shape oscillations [12,13]. Electrostatic levitation, in which a charged sample is levitated in between vertically oriented parallel electrodes, also has been used for measuring the properties of molten materials [14–16]. A heating device is necessary to keep the material temperature constant for liquid metal, but electrostatic levitation without heating has been used for observing crystal growth processes [17] and for measurement of organic solvent [18]. Aerodynamic levitation was proposed to measure the material properties of corium, which is the molten mixture of nuclear fuels, for numerical simulations of nuclear accidents [19]. The objects levitated by acoustic forces have been used for exploring chemical and biological processes such as microreactors [20] and for manipulating cells and drugs without touching or contaminating them [21]. Large deformation of a droplet due to increasing sound intensity has been studied experimen-

tally and numerically [22]. The progress and application of acoustic levitation were reviewed in [23].

The dynamics of levitated or free droplets including shape oscillations has been studied by many researchers for applications such as measurement of material properties and for understanding of droplet physics [24]. The surface tension was obtained based on the linear theory [25], in which the oscillation amplitude was assumed to be small. The oscillation frequency was shown to decrease with increasing amplitude [26–29] and numerical simulations were performed [30,31]. Nonlinear oscillations with higher-order oscillation modes have been discussed [32–40] along with the frequency shift. The effect of rotation on the droplet has been studied theoretically and the stability of equilibrium shape [41,42], the frequency shift [43,44], and the viscous damping [45] have been discussed. The frequency shift and the viscous damping also have been observed experimentally [46] and calculated [47–49].

As for the shapes, the droplet evolves from a sphere to an ellipsoid with increasing rotation rate. The axisymmetric shape becomes unstable and the nonaxisymmetric shape appears, which is elongated with decreasing rotation rate. The nonaxisymmetric shape then becomes a two-lobed (dumbbell) shape. The axisymmetric shapes have been discussed theoretically in relation to atomic nuclei [50]. The equilibrium shapes have been calculated numerically and the axisymmetric, two-, three-, and four-lobed shapes were shown by taking into account the surface energy and the rotation energy [51,52]. The bifurcation from axisymmetric to two-lobed shapes was observed experimentally and compared with the calculated results [53]. The axisymmetric, nonaxisymmetric, and two-lobed shapes were experimentally studied by solidifying rotating liquid droplets [54]. The deformation of the two-lobed shape was evaluated based on the radius of the central cross section [55] and the theoretical model for representing the two-lobed shape was discussed [56]. It was proposed that the transient of two-lobed shape could be used for measuring the viscosity of molten material with the viscosity range from 0.1 to 100 Pa s [18]. Transient variations including axisymmetric and two-lobed shapes were studied in relation to the formation of natural tektites [57] and simulated [58–60].

In this study, the transient shape variation of a rotating droplet is simulated numerically using the experimental conditions in [18] and the relation between the deformation and the rotation rate is discussed by comparing with the experimental data. The flow field in the two-lobed droplet is shown and the effects of viscosity, surface tension, and density are discussed.

II. NUMERICAL CONDITIONS

The flow field including a rotating droplet is simulated using the level set method [61], and the governing equations and the numerical method are described in Appendixes A and B, respectively. The numerical conditions are based on the experimental conditions in [18]. In the experiment, electrostatic levitation was used and the levitated droplet was rotated around the vertical center axis by the acoustic standing wave in the horizontal direction. The transient shape variation of the two-lobed droplet was observed by the line sensor and the viscosity was obtained from the time variation of the minimum diameter which was in the central cross section in between two lobes. The outline of the simulation region and the rotating droplet is shown in Fig. 1. The simulation region is a three-dimensional rectangular region with a size of $14.1 \times 14.1 \times 7.7\,\mathrm{mm}^3$, which was determined by preliminary sensitivity calculations shown in Appendix C. Periodic boundary conditions are applied on all sides of the simulation region. A spherical droplet with a radius of 2.0 mm is located in the center of the simulation region. Propylene carbonate (with density ρ, viscosity η, and surface tension γ of $1206\,\mathrm{kg/m}^3$, 0.0026 Pa s, and 0.043 N/m, respectively) and air ($\rho = 1.166\,\mathrm{kg/m}^3$ and $\eta = 1.819 \times 10^{-5}$Pas) are assumed for the inside and outside properties of the droplet, respectively. A rotation rate of 30 rps is imposed on the droplet initially as a rigid rotation around the vertical center axis. The droplet Reynolds number, Weber number, and capillary number are initially about 700, 16, and 0.023, respectively. The droplet shape becomes an ellipsoid, then a nonaxisymmetric shape, and finally a two-lobed shape. The two-lobed droplet is elongated gradually and breaks up.

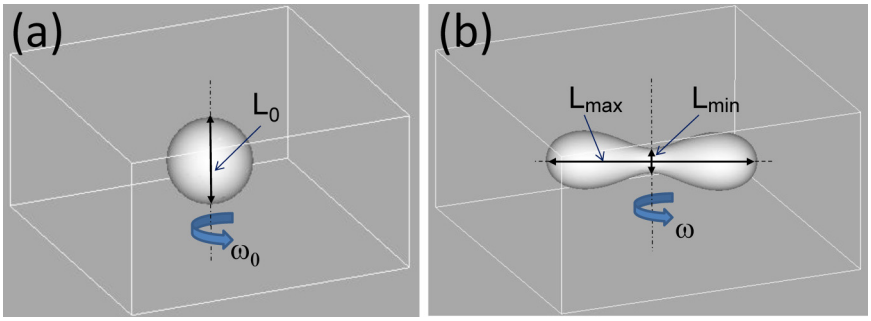

FIG. 1. Outline of the simulation region and rotating droplet: (a) initial condition and (b) two-lobed shape.

The number of calculation mesh cells and the grid size are determined in Appendix C so that the dynamics of the two-lobed droplet is not affected by these numerical conditions. The maximum Courant number is smaller than 0.1 throughout the calculations.

The resonant angular velocity $\omega_0 = \sqrt{64\gamma/\rho L_0^3}$ is used for nondimensional parameters in the following section and Appendix C. It is about 188.8 rad/s, and the initial rotation of 30 rps corresponds to it.

III. RESULTS AND DISCUSSION

A. Shape variation

The calculated shapes of the two-lobed droplet at different timings are shown in Fig. 2, where the steady-state calculations in [62] are also indicated by dashed lines. The two-lobed droplets are obtained at nondimensional times of 49.6 and 56.5 in Figs. 2(a) and 2(b), respectively. The nondimensional rotation rates at these timings are 0.37 and 0.28, respectively. The steady-state shapes shown by the dashed lines were calculated with rotation rates of 0.3790 and 0.2885, respectively [62]. The transient but slow process is necessary for the viscosity measurement using the two-lobed shape. It is shown in Fig. 2 that the present transient results agree with the steady-state results in terms of the droplet shape and the transient process is sufficiently slow.

The simulation results are compared with the existing experimental results in Fig. 3. The maximum deformation is plotted against the rotation rate in Fig. 3(a), where the rotation rate is nondimensionalized by the resonant angular velocity ω_0. The maximum deformation is obtained as the maximum distance between two surface cells, which include the droplet surface, and the rotation rate is calculated as the time variation of its rotation angle. The maximum deformation oscillates slightly even after the initial transient, as shown in Fig. 9 in Appendix C, and the calculated rotation rate also oscillates. Each simulation point shown in Fig. 3 is thus obtained as the average over the nondimensional time of 0.6. The experimental results with smaller deformation are shown to be larger than the simulation results in Fig. 3(a). The simulated droplet is under the transient condition

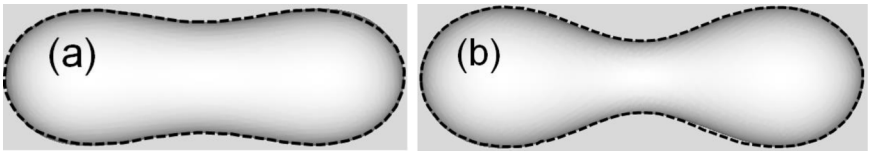

FIG. 2. Two-lobed droplet shape at the nondimensional time of (a) 49.6 and (b) 56.5. The nondimensional rotation rates at these timings are (a) 0.37 and (b) 0.28. The outlines indicated by dashed lines correspond to the calculated results for the steady state with a rotation rate of (a) 0.3790 and (b) 0.2885 in [62].

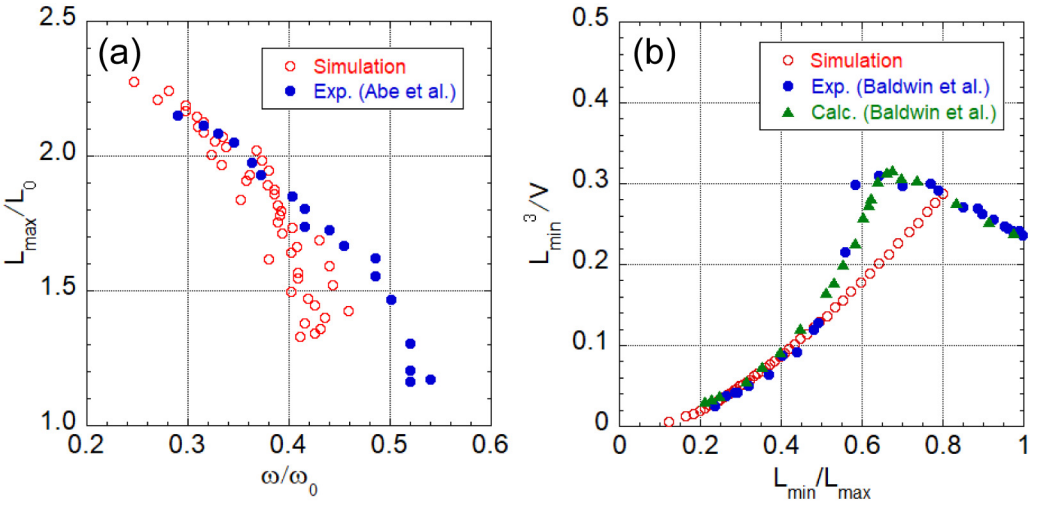

FIG. 3. Comparison with experimental results: (a) the maximum deformation L_{max}/L_0 plotted against the rotation rate ω/ω_0 [18] and (b) the deformation parameter L_{min}^3/V plotted against the aspect ratio L_{min}/L_{max} [54] along with the calculated results in [54].

and the nonaxisymmetric shape is still affected by the initial condition. The simulation results, however, agree with the experimental results for large deformation of a two-lobed droplet with the maximum deformation larger than 1.8.

The deformation parameter L_{min}^3/V is plotted against the aspect ratio of the droplet in Fig. 3(b). The deformation parameter is a cube of minimum diameter L_{min} in Fig. 1, nondimensionalized by the volume of droplet V. The minimum diameter is the diameter of the central cross section of a nonaxisymmetric or two-lobed droplet as shown in Fig. 1 and the aspect ratio is defined by L_{min}/L_{max}. The experimental data and the calculated results in [54] are also plotted in Fig. 3(b). Magnetic levitation was used in the experiment, and air flow in the horizontal direction was used for rotation [54]. The rotating droplet of molten wax was solidified by rapid cooling, and the shape of solidified droplet, which was an artificial tektite, was measured. The axisymmetric shape was observed in the experiment for the aspect ratio larger than 0.67, while the nonaxisymmetric shape was seen for the aspect ratio smaller than 0.67. It was also reported that the two-lobed shape was observed for the aspect ratio smaller than 0.45. The two-lobed shape was shown to be obtained theoretically for the aspect ratio smaller than 0.52 [56]. The experimental and calculated results for the nonaxisymmetric shape in [54] are shown to be larger than the simulation results. The simulated droplets are still affected by the initial condition as seen in Fig. 3(a). The simulation results are however found to agree with the experimental and calculated results for the two-lobed shape in [54].

In this study, the initial rotation is numerically imposed on the spherical droplet, while an acoustic force and air flows were used in the experiments in Figs. 3(a) and 3(b), respectively, to rotate the spherical droplet. The calculated results in Figs. 2 and 3(b) were obtained for the steady-state rotation with specified rotation rates. Although the driving force and the method for rotation were different, the present simulation was confirmed to reproduce the shape variation of a rotating two-lobed droplet.

B. Inner flow field

The inner flow field of a two-lobed droplet is discussed here, since the flow condition is of importance for the viscosity measurement using the two-lobed droplet. The flow field at the nondimensional time of 57.1 is shown in Fig. 4, where the droplet shape and the velocity vector are

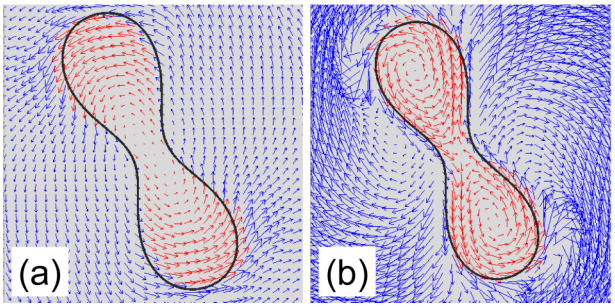

FIG. 4. Droplet shape and velocity vector at the nondimensional time of 57.1: (a) the flow field in the fixed coordinate and (b) the flow field in the rotating coordinate.

shown in the horizontal cross section at the vertical midelevation. The nondimensional rotation rate and the aspect ratio for the two-lobed shape shown in Fig. 4 are about 0.26 and 0.14, respectively, and the Reynolds number, Weber number, and capillary number are estimated to be about 920, 12, and 0.013, respectively. The droplet is rotating counterclockwise in Fig. 4 and the rotating flow field is shown in Fig. 4(a) with the rotation axis at the center of the droplet. The velocity vector shown in Fig. 4(b) is obtained by subtracting the rotation rate of the droplet from the velocity vector shown in Fig. 4(a). The flow field shown in Fig. 4(a) thus corresponds to the flow field in the fixed coordinate and that in Fig. 4(b) to the flow field in the rotating coordinate. The vector scale is four times larger in Fig. 4(b) to see clearly the flow field. It is found in the inner flow field shown in Fig. 4(b) that two vortices are formed in the two-lobed droplet. Each vortex is in each lobe and the rotation of the vortex is counterclockwise for both vortices. The countercurrent flow appears in between two lobes at around the rotation axis of the droplet. The measurement of viscosity using the rotating two-lobed droplet is based on a filament rheometer [63,64] and it might be necessary to evaluate the effect of countercurrent flow in between two lobes.

The transient variations from the nonaxisymmetric shape to the two-lobed shape are shown in Fig. 5. The velocity vectors in the rotating coordinate are also indicated in Fig. 5. The droplet shape and velocity vectors in Figs. 5(a), 5(b), 5(c), and 5(d) are obtained at nondimensional times of 34.6, 39.1, 43.6, and 48.1, respectively. A single vortex is seen in Fig. 5(a) and the vortex center corresponds to the rotation axis of the droplet. The rotation of the vortex is counterclockwise and the same as that of the droplet. In Figs. 5(b) and 5(c) the vortex is elongated according to the shape variation and the vortex center is also elongated. Two vortices appear in the two-lobed shape in Fig. 5(d). It is indicated that the single vortex is elongated and becomes two vortices as the nonaxisymmetric shape becomes the two-lobed shape (nonaxisymmetric shapes with concave central parts). The two vortices are thus rotating counterclockwise and the countercurrent flow

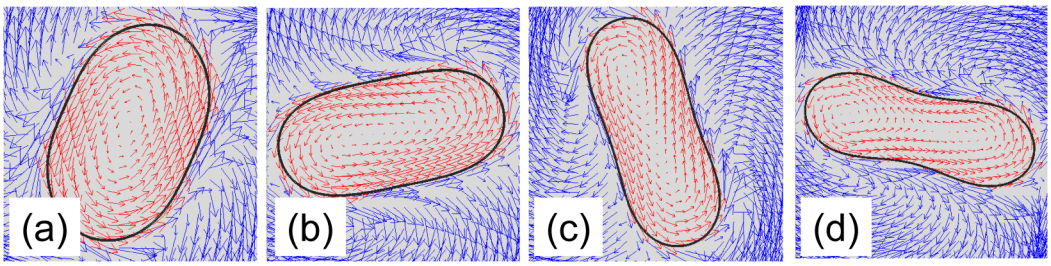

FIG. 5. Transient variations of droplet shape and velocity vector at the nondimensional time of (a) 34.6, (b) 39.1, (c) 43.6, and (d) 48.1.

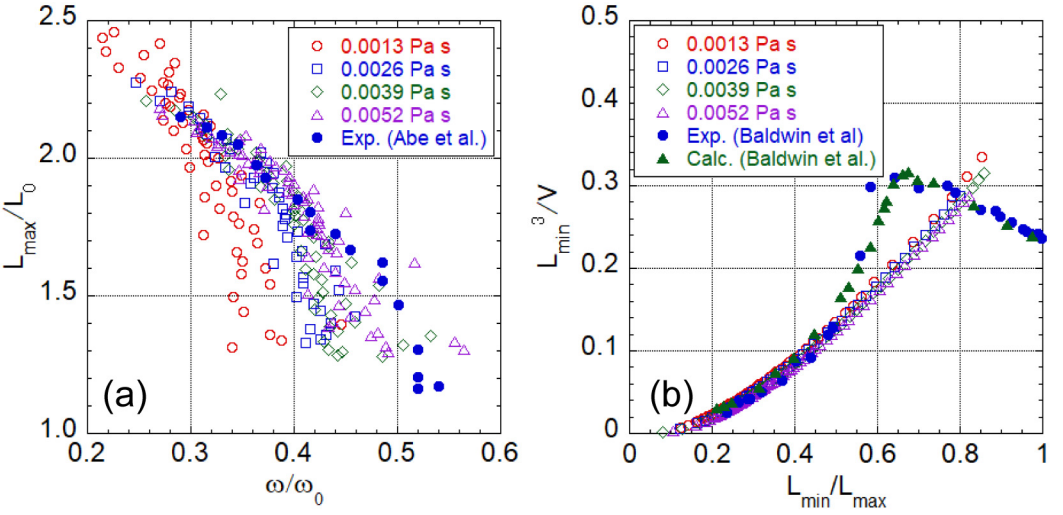

FIG. 6. Effect of viscosity: (a) the maximum deformation L_{max}/L_0 plotted against the rotation rate ω/ω_0 and (b) the deformation parameter L_{min}^3/V plotted against the aspect ratio L_{min}/L_{max}.

appears in between two lobes as shown in Fig. 4(b). The aspect ratios of the droplets are about 0.64, 0.48, 0.38, and 0.30 in Figs. 5(a), 5(b), 5(c), and 5(d), respectively. The relation between the droplet shape and the aspect ratio shown in Fig. 5 corresponds to the experimental results in [54].

C. Effects of viscosity, surface tension, and density

Sensitivity calculations, in which one parameter is changed and the other numerical conditions are the same, are performed and the effects of viscosity, surface tension, and density on the two-lobed droplet are discussed. The effects of viscosity are shown in Fig. 6, where the simulation cases with viscosities of 0.0013, 0.0026, 0.0039, and 0.0052 Pa s are indicated along with the experimental results with a viscosity of 0.0026 Pa s. The maximum deformation against the rotation rate is shown in Fig. 6(a), while the deformation parameter against the aspect ratio is in Fig. 6(b). The dispersion for the small viscosity case of 0.0013 Pa s is larger than that for other cases in Fig. 6(a), since the effect of the initial shape oscillation remains for a longer time. The dispersion for large deformation is however small for other cases, and the effects of viscosity on the maximum deformation are shown to be small in Fig. 6(a), since the two-lobed shape is observed under slow transient conditions with gradual elongation. The measurement of viscosity using the rotating two-lobed droplet is performed under these conditions, and thus the inner flow field shown above would be important. The deformation parameter in Fig. 6(b) is not affected by the viscosity and all the cases with different viscosity agree with the experimental and calculated results in [54] for the two-lobed shape.

The effects of surface tension on the maximum deformation and the deformation parameter are shown in Figs. 7(a) and 7(b), respectively, where the simulation cases with surface tensions of 0.035, 0.043, 0.052, and 0.060 N/m are indicated along with the experimental results with a surface tension of 0.043 N/m. The maximum deformation in Fig. 7(a) is shown to be affected by the surface tension even for large deformation, in contrast to the effect of viscosity shown in Fig. 6(a). It is found for the same deformation that a higher rotation rate is necessary for higher surface tension. This indicates that the surface tension is balanced with the elongation due to rotation. The effect of surface tension should thus be taken into account for the measurement of viscosity using the rotating two-lobed droplet. The deformation parameter shown in Fig. 7(b) is however not affected

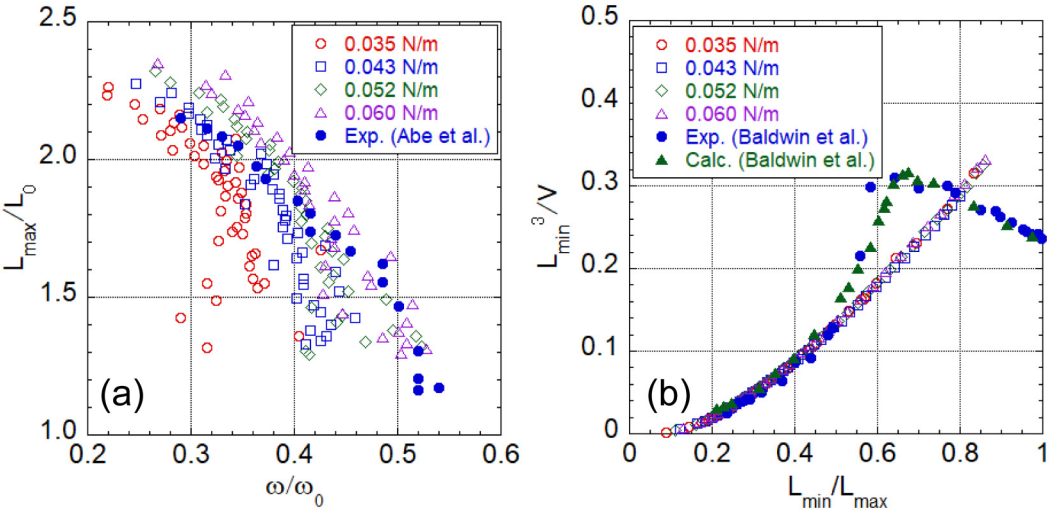

FIG. 7. Effect of surface tension: (a) the maximum deformation L_{max}/L_0 plotted against the rotation rate ω/ω_0 and (b) the deformation parameter L_{min}^3/V plotted against the aspect ratio L_{min}/L_{max}.

by the surface tension and all the cases with different surface tension agree with the experimental and calculated results in [54] for the two-lobed shape.

The effects of density on the maximum deformation and the deformation parameter are shown in Figs. 8(a) and 8(b), respectively, where the simulation cases with densities of 800, 1000, 1206, and 1400 $\mathrm{kg/m^3}$ are indicated along with the experimental results with a density of 1206 $\mathrm{kg/m^3}$. The effects of density on the maximum deformation are large for small deformation and small for large deformation, as shown in Fig. 8(a). It is seen for the same deformation that a higher rotation rate is necessary for smaller density, since the centrifugal force depends on the density and the rotation rate. It is noted that the simulation results with different density seem to be converged to

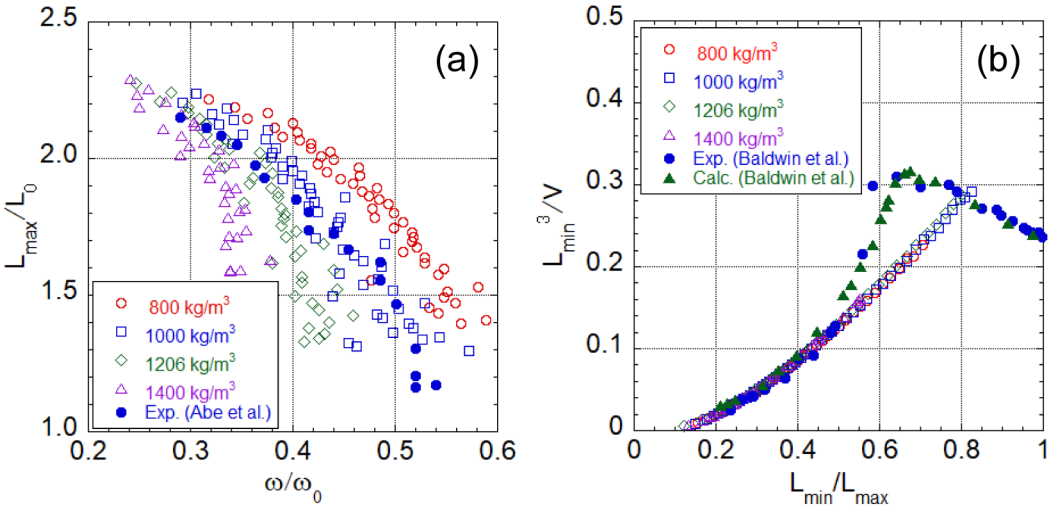

FIG. 8. Effect of density: (a) the maximum deformation L_{max}/L_0 plotted against the rotation rate ω/ω_0 and (b) the deformation parameter L_{min}^3/V plotted against the aspect ratio L_{min}/L_{max}.

the point with the largest deformation. In other words, the maximum deformation is affected by the density, but the effect of density becomes small as the maximum deformation increases, in contrast to the effect of surface tension shown in Fig. 7(a). The effect of density should also be taken into account for the measurement of viscosity using the rotating two-lobed droplet. The deformation parameter shown in Fig. 8(b) is not affected by the density and all the cases with different density agree with the experimental and calculated results in [54] for the two-lobed shape. It is thus found from Figs. 6(b), 7(b), and 8(b) that the relation between the deformation parameter and the aspect ratio is not affected by the droplet properties.

IV. CONCLUSION

The transient shape variation and the inner flow field of a rotating liquid droplet have been obtained in this study by solving the Navier-Stokes equations using the level set method. The calculated two-lobed shapes were shown to agree with the experimental and calculated results obtained under steady-state conditions [54,62]. It was also shown that the relation between the maximum deformation and the rotation rate agreed with the experimental results [18]. It was found that two vortices appeared in the two-lobed droplet, while a single vortex was formed in the nonaxisymmetric droplet. The vortex in the nonaxisymmetric droplet was elongated and two vortices were formed as the nonaxisymmetric droplet became the two-lobed droplet. The countercurrent flow was found in between two lobes. The relation between the maximum deformation and the rotation rate was affected by the surface tension and the density, and the effect of density became small as the deformation increased. It might thus be necessary to evaluate the effects of countercurrent flow, the surface tension, and the density for the viscosity measurement using the two-lobed droplet. In contrast, the relation between the deformation parameter based on the minimum diameter and the aspect ratio was not affected by the droplet properties such as the viscosity, the surface tension, and the density.

The shape variation and the inner flow field of rotating liquid droplets are of importance not only for the viscosity measurement using the two-lobed droplet but also for the application using levitated liquid droplets such as in chemical and biological processes, cell and drug manipulations, and tektite formation. The simulation results obtained in this study would be useful for wide application.

APPENDIX A: GOVERNING EQUATION

The flow field including a rotating droplet is simulated using the level set method [61] and the numerical model is described briefly here. The flow fields in and around the droplet are described by the equation of continuity and the incompressible Navier-Stokes equations

$$\nabla \cdot \boldsymbol{u} = 0 \tag{A1}$$

and

$$\rho \frac{D\boldsymbol{u}}{Dt} = -\nabla p + \nabla \cdot (2\eta \boldsymbol{D}) - \boldsymbol{F}_s, \tag{A2}$$

where ρ, $\boldsymbol{u}$, p, and η are the density, the velocity, the pressure, and the viscosity, respectively, $\boldsymbol{D}$ is the viscous stress tensor, and $\boldsymbol{F}_s$ is a body force due to the surface tension. External force fields used in the experiments are not simulated in this study since the numerical calculations [51,54,62] did not take external forces into account and the good agreement with the experimental and calculated results was shown. The surface tension force is given by

$$\boldsymbol{F}_s = \gamma \kappa \delta \nabla \phi, \tag{A3}$$

where γ, κ, δ, and ϕ are the surface tension, the curvature of the interface, the Dirac delta function, and the level set function, respectively. The level set function is a distance function defined as the

normal distance from the interface: $\phi = 0$ at the interface, $\phi < 0$ in the liquid region, and $\phi > 0$ in the gas region. The curvature of the interface is expressed in terms of ϕ:

$$\kappa = \nabla \cdot \left(\frac{\nabla \phi}{|\nabla \phi|} \right) \tag{A4}$$

The density and viscosity are given, respectively, by

$$\rho = \rho_l + (\rho_g - \rho_l) H \tag{A5}$$

and

$$\eta = \eta_l + (\eta_g - \eta_l) H, \tag{A6}$$

where the subscripts g and l indicate gas and liquid phases, respectively. In Eqs. (A5) and (A6), H is the smoothed function similar to the Heaviside function, defined by

$$H = \begin{cases} 0 & (\phi < -\varepsilon) \\ \frac{1}{2}\left[1 + \frac{\phi}{\varepsilon} + \frac{1}{\pi} \sin\left(\frac{\pi \phi}{\varepsilon}\right)\right] & (-\varepsilon \leqslant \phi \leqslant \varepsilon) \\ 1 & (\varepsilon < \phi), \end{cases} \tag{A7}$$

where ε is a small positive constant for which $|\nabla \phi| = 1$ for $|\phi| \leqslant \varepsilon$. The evolution of ϕ is given by

$$\frac{D\phi}{Dt} = 0. \tag{A8}$$

In order to maintain the level set function as a distance function, reinitialization of the level set function is proposed by solving the equation

$$\frac{\partial \phi}{\partial \tau} = \mathrm{sgn}(\phi_0)(1 - |\nabla \phi|), \tag{A9}$$

where τ is an artificial time and $\mathrm{sgn}(\phi_0)$ indicates the sign of the level set function at the beginning of the reinitialization procedure. The level set function becomes a distance function ($|\nabla \phi| = 1$) in the steady-state solution ($\frac{\partial \phi}{\partial \tau} = 0$) of Eq. (A9). The smoothed sign function proposed for numerical treatment of reinitialization is used:

$$\mathrm{sgn}(\phi_0) = \frac{\phi_0}{\sqrt{\phi_0^2 + \varepsilon^2}}. \tag{A10}$$

The following equation is also solved to preserve the total mass in time [65]:

$$\frac{\partial \phi}{\partial \tau} = (A_0 - A)(P - \kappa)|\nabla \phi|. \tag{A11}$$

Here A_0 denotes the total mass for the initial condition and A denotes the total mass corresponding to the level set function. In addition, P is a positive constant for stabilization and 1.0 was used. In Eq. (A11), τ is an artificial time and the total mass is conserved ($A_0 = A$) in the steady-state solution ($\frac{\partial \phi}{\partial \tau} = 0$). Equations (A9) and (A11) are additional equations for modification of the level set function at the new time level.

APPENDIX B: NUMERICAL METHOD

The finite difference method is used to solve the governing equations. The staggered mesh system is used for spatial discretization of velocities. The convection terms are discretized using the second-order upwind scheme and other terms by the second-order central difference scheme. Time integration is performed by the second-order Adams-Bashforth method. The simplified marker

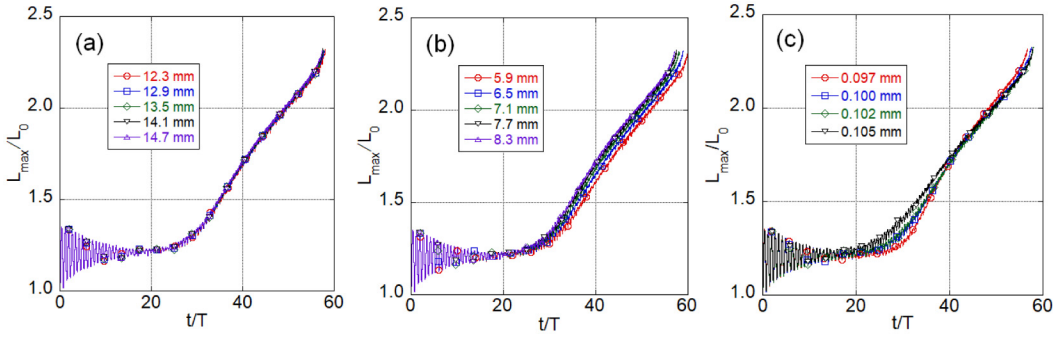

FIG. 9. Time variation of maximum deformation. The effects of region size are indicated for (a) the horizontal direction and (b) the vertical direction. (c) Effects of grid size.

and cell method is used to obtain pressure and velocities [66]. The pressure Poisson equation is solved using the biconjugate gradient stabilized (Bi-CGSTAB) method. The domain decomposition technique is applied and the mpi library is used for parallel computations, and the block Jacobi preconditioner is used for the parallel Bi-CGSTAB method [67].

APPENDIX C: CONVERGENCE OF NUMERICAL RESULTS

The maximum deformation $L_{\max}$ in Fig. 1(b), which is defined as the longest straight line between two points on the surface in the horizontal cross section at the vertical midelevation, is shown in Fig. 9. The maximum deformation is nondimensionalized by the initial diameter L_0 and the time t is nondimensionalized by the resonant period T, which is given by $2\pi/\omega_0$. The effects of simulation region size are also indicated in Fig. 9. The simulation region size ranges from 12.3 to 14.7 mm in the horizontal direction in Fig. 9(a) with a vertical size of 7.7 mm and from 5.9 to 8.3 mm in the vertical direction in Fig. 9(b) with a horizontal size of 14.1 mm. The grid size is fixed at 0.1 mm in Figs. 9(a) and 9(b) and the number of mesh cells is changed in these sensitivity calculations. The effects of region size are small enough for $14.1 \times 14.1 \times 7.7\text{mm}^3$, as shown in Figs. 9(a) and 9(b), and this size is used in this study. The grid size ranges from 0.097 to 0.105 mm in Fig. 9(c) with the same number of mesh cells: $141 \times 141 \times 77$. The simulation region size is thus slightly changed in Fig. 9(c). The effects of grid size are seen at around the nondimensional time of about 30, where the droplet becomes a nonaxisymmetric shape. The increase in maximum deformation is however not affected afterward for the two-lobed droplet and the grid size of 0.1 mm is used in this study.

The maximum deformation is unity initially and becomes large and oscillates around the value of 1.2 as shown in Fig. 9 due to the imposed rotation. The value of 1.2 corresponds to the smallest value for the nonaxisymmetric shape in the experiment as shown in Fig. 3(a) and this value may show an unstable state for the transition to the nonaxisymmetric shape. The maximum deformation increases after the nondimensional time of about 25 and the droplet becomes a nonaxisymmetric shape. The nonaxisymmetric shape gradually becomes the two-lobed shape as the maximum deformation increases. The two-lobed shape appears at the nondimensional time of about 43 with a maximum deformation of about 1.8. The two-lobed shape is finally broken up at the nondimensional time of about 58 in Fig. 9.

[1] S. Sauerland, G. Lohoefer, and I. Egry, Surface tension measurements on levitated aspherical liquid nickel drops, Thermochim. Acta **218**, 445 (1993).

[2] I. Egry, G. Lohoefer, and G. Jacobs, Surface Tension of Liquid Metals: Results from Measurements on Ground and in Space, Phys. Rev. Lett. **75**, 4043 (1995).

[3] M. Przyborowski, T. Hibiya, M. Eguchi, and I. Egry, Surface tension measurement of molten silicon by the oscillating drop method using electromagnetic levitation, J. Cryst. Growth **151**, 60 (1995).
[4] M. Roesner-khun, W. H Hofmeister, G. Kuppermann, R. J. Bayuzick, and M. G. Frohberg, Investigations of the influence of oxygen on the surface tension of zirconium by the oscillating drop technique, Surf. Sci. **443**, 159 (1999).
[5] I. Egry and S. Sauerland, Containerless processing of undercooled melts: Measurements of surface tension and viscosity, Mater. Sci. Eng. A **178**, 73 (1994).
[6] I. Egry, Structure and properties of levitated liquid metals, J. Non-Cryst. Solids. **250–252**, 63 (1999).
[7] H. Fujii, T. Matsumoto, and K. Nogi, Analysis of surface oscillation of droplet under microgravity for the determination of its surface tension, Acta Mater. **48**, 2933 (2000).
[8] D. L. Cummings and D. A. Blackburn, Oscillations of magnetically levitated aspherical droplets, J. Fluid Mech. **224**, 395 (1991).
[9] A. Bratz and I. Egry, Surface oscillations of electromagnetically levitated viscous metal droplets, J. Fluid Mech. **298**, 341 (1995).
[10] V. Shatrov, J. Priede, and G. Gerbeth, Three-dimensional linear stability analysis of the flow in a liquid spherical droplet driven by an alternating magnetic field, Phys. Fluids **15**, 668 (2003).
[11] K. Im and Y. Mochimaru, Numerical analysis on magnetic levitation of liquid metals, using a spectral finite difference scheme, J. Comput. Phys. **203**, 112 (2005).
[12] R. J. A. Hill and L. Eaves, Vibrations of a diamagnetically levitated water droplet, Phys. Rev. E **81**, 056312 (2010).
[13] R. J. A. Hill and L. Eaves, Shape oscillations of an electrically charged diamagnetically levitated droplet, Appl. Phys. Lett. **100**, 114106 (2012).
[14] P.-F. Paradis, T. Ishikawa, and N. Koike, Non-contact measurements of the surface tension and viscosity of molybdenum using an electrostatic levitation furnace, Int. J. Refract. Met. Hard Mater. **25**, 95 (2007).
[15] P.-F. Paradis, T. Ishikawa, N. Koike, and Y. Watanabe, Physical properties of liquid terbium measured by levitation techniques, J. Rare Earths **25**, 665 (2007).
[16] J. Okada, T. Ishikawa, Y. Watanabe, and P. Paradis, Surface tension and viscosity of molten vanadium measured with an electrostatic levitation furnace, J. Chem. Thermodyn. **42**, 856 (2010).
[17] W. K. Rhim and S. K. Chung, Isolation of crystallizing droplets by electrostatic levitation, Methods **1**, 118 (1990).
[18] Y. Abe, S. Matsumoto, T. Watanabe, K. Nishinari, H. Kitahata, A. Kaneko, K. Hasegawa, R. Tanaka, K. Shitanishi, and S. Sasaki, Nonlinear dynamics of levitated droplet, Int. J. Microgravity Sci. Appl. **30**, 42 (2013).
[19] E. Herview, N. Coutris, and C. Boichon, Oscillations of a drop in aerodynamic levitation, Nucl. Eng. Design **204**, 167 (2001).
[20] A. Scheeline and R. Behrens, Potential of levitated drops to serve as microreactors for biophysical measurements, Biophys. Chem. **165–166**, 1 (2012).
[21] A. Marzo, S. A. Seah, B. W. Drinkwater, D. R. Sahoo, B. Long, and S. Subramanian, Holographic acoustic elements for manipulation of levitated objects, Nat. Commun. **6**, 8661 (2015).
[22] W. Di, Z. Zhang, L. Lin, J. Li, X. Li, B. P. Binks, X. Chen, and D. Zang, Shape evolution and bubble formation of acoustically levitated drops, Phys. Rev. Fluids **3**, 103606 (2018).
[23] M. A. B. Andrade, N. Perez, and J. C. Adamowski, Review of progress in acoustic levitation, Braz. J. Phys. **48**, 190 (2018).
[24] T. G. Wang, Equilibrium shapes of rotating spheroids and drop shape oscillations, Adv. Appl. Mech. **26**, 1 (1988).
[25] H. Lamb, *Hydrodynamics* (Cambridge University Press, Cambridge, 1932).
[26] E. H. Trinh and T. G. Wang, Large-amplitude free and driven drop-shape oscillations: Experimental observations, J. Fluid Mech. **122**, 315 (1982).
[27] E. H. Trinh, A. Zwern, and T. G. Wang, An experimental study of small-amplitude drop oscillations in immiscible liquid systems, J. Fluid Mech. **115**, 453 (1982).
[28] J. A. Tsamopoulos and R. A. Brown, Nonlinear oscillations of inviscid drops and bubbles, J. Fluid Mech. **127**, 519 (1983).

[29] J. Q. Feng and K. V. Beard, Three-dimensional oscillation characteristics of electrostatically deformed drops, J. Fluid Mech. **227**, 429 (1991).
[30] G. B. Foote, A numerical method for studying liquid drop behavior: Simple oscillation, J. Comput. Phys. **11**, 507 (1973).
[31] H. M. Duerr and J. Siekmann, Numerical studies of fluid oscillation problems by boundary integral techniques, Acta Astronaut. **15**, 859 (1987).
[32] R. Natarajan and R. A. Brown, Third-order resonance effects and the nonlinear stability of drop oscillations, J. Fluid Mech. **183**, 95 (1987).
[33] T. S. Lundgren and N. N. Mansour, Oscillations of drops in zero gravity with weak viscous effects, J. Fluid Mech. **183**, 95 (1988).
[34] E. Becker, W. J. Hiller, and T. A. Kowalewski, Nonlinear dynamics of viscous droplets, J. Fluid Mech. **258**, 191 (1994).
[35] E. Becker, W. J. Hiller, and T. A. Kowalewski, Experimental and theoretical investigation of large-amplitude oscillations of liquid droplets, J. Fluid Mech. **231**, 189 (1991).
[36] E. H. Trinh, D. B. Thiessen, and R. G. Holt, Driven and freely decaying nonlinear shape oscillations of drops and bubbles immersed in a liquid: experimental results, J. Fluid Mech. **364**, 253 (1998).
[37] H. Azuma and S. Yoshihara, Three-dimensional large-amplitude drop oscillations; experiments and theoretical analysis, J. Fluid Mech. **393**, 309 (1999).
[38] T. W. Patzek, O. A. Basaran, R. E. Benner, and L. E. Scriven, Nonlinear oscillations of two-dimensional, rotating inviscid drops, J. Comput. Phys. **116**, 3 (1995).
[39] O. A. Basaran, Nonlinear oscillations of viscous liquid drops, J. Fluid Mech. **241**, 169 (1992).
[40] X. Chen, T. Shi, Y. Tian, J. Jankovsky, G. Holt, and R. E. Apfel, Numerical simulation of superoscillations of a Triton-bearing drop in microgravity, J. Fluid Mech. **367**, 205 (1998).
[41] S. Chandrasekhar, The stability of a rotating liquid drop, Proc. R. Soc. London Ser. A **286**, 1 (1965).
[42] S. Malik, O. M. Lavrenteva, and A. Nir, Shapes and stability of viscous rotating drops in a compressional/extensional flow, Phys. Rev. Fluids **5**, 023604 (2020).
[43] F. H. Busse, Oscillations of a rotating liquid drop, J. Fluid Mech. **142**, 1 (1984).
[44] H. Kitahata, R. Tanaka, Y. Koyano, S. Matsumoto, K. Nishinari, T. Watanabe, K. Hasegawa, T. Kanagawa, A. Kaneko, and Y. Abe, Oscillation of a rotating levitated droplet: Analysis with a mechanical model, Phys. Rev. E **92**, 062904(2015).
[45] C. P. Lee, M. J. Lyell, and T. G. Wang, Viscous damping of the oscillations of a rotating simple drop, Phys. Fluids **28**, 3187 (1985).
[46] P. Annamalai, E. Trinh, and T. G. Wang, Experimental study of the oscillations of a rotating drop, J. Fluid Mech. **158**, 317 (1985).
[47] T. Watanabe, Numerical simulation of oscillations and rotations of a free liquid droplet using the level set method, Comput. Fluids **37**, 91 (2008).
[48] T. Watanabe, Zero frequency shift of an oscillating-rotating liquid droplet, Phys. Lett. A **372**, 482 (2008).
[49] T. Watanabe, Frequency shift and aspect ratio of a rotating-oscillating liquid droplet, Phys. Lett. A **373**, 867 (2009).
[50] S. Cohen, F. Plasil, and W. J. Swiatecki, Equilibrium configurations of rotating charged or gravitating liquid masses with surface tension. II, Ann. Phys. (N.Y.) **82**, 557 (1974).
[51] R. A. Brown and L. E. Scriven, The shape and stability of rotating liquid drops, Proc. R. Soc. London Ser. A **371**, 331 (1980).
[52] C.-J. Heine, Computations of form and stability of rotating drops with finite elements, IMA J. Numer. Anal. **26**, 723 (2006).
[53] T. G. Wang, A. V. Anilkumar, C. P. Lee, and K. C. Lin, Bifurcation of rotating liquid drops: Results from USML-1 experiments in space, J. Fluid Mech. **276**, 389 (1994).
[54] K. A. Baldwin, S. L. Butler, and R. J. A. Hill, Artificial tektites: An experimental technique for capturing the shapes of spinning drops, Sci. Rep. **5**, 7660 (2015).
[55] P. Aussillous and D. Quere, Shapes of rolling liquid drops, J. Fluid Mech. **512**, 133 (2004).
[56] H. Ishikawa and K. Nishinari, Modelling levitated 2-lobed droplets in rotation using Cassinian oval curves, J. Fluid Mech. **846**, 1088 (2018).

[57] L. T. Elkins-tanton, P. Aussillous, J. Bico, D. Quere, and J. W. M. Bush, A laboratory model of splash-form tektites, Meteorit. Planet. Sci. **38**, 1331 (2003).
[58] T. W. Patzek, R. E. Benner, O. A. Basaran, and L. E. Scriven, Nonlinear oscillations of inviscid free droplets, J. Comput. Phys. **97**, 489 (1991).
[59] M. R. Stauffer and S. L. Butler, The shapes of splash-form tektites; their geometrical analysis, classification and mechanics of formation, Earth Moon Planets **107**, 169 (2010).
[60] T. Watanabe, Deformation of a rotating two-lobed droplet, Int. J. Math. Models Methods Appl. Sci. **10**, 179 (2016).
[61] M. Sussman, P. Smereka, and S. Osher, A level set approach for computing solutions to incompressible two-phase flow, J. Comput. Phys. **114**, 146 (1994).
[62] C.-J. Heine, Computations of form and stability of rotating drops with finite elements, Ph.D. thesis, RWTH Aachen University, 2003.
[63] P. Szabo, Transient filament stretching rheometer I: Force balance analysis, Rheol. Acta **36**, 277 (1997).
[64] G. H. McKinley and A. Tripathi, How to extract the Newtonian viscosity from capillary breakup measurements in a filament rheometer, J. Rheol. **44**, 653 (2000).
[65] Y. C. Chang, T. Y. Hou, B. Merriman, and S. Osher, A level set formulation of Eulerian interface capturing methods for incompressible fluid flows, J. Comput. Phys. **124**, 449 (1996).
[66] A. A. Amsden and F. H. Harlow, Simplified MAC technique for incompressible fluid flow calculations, J. Comput. Phys. **6**, 322 (1970).
[67] T. Watanabe, in *Parallel Computations of Droplet Oscillations*, edited by I. H. Tuncer, Ü. Gülcat, D. R. Emerson, and K. Matsuno, Lecture Notes in Computer Science and Engineering Vol. 67 (Springer, Berlin, 2009), p. 163.